doi:10.26443/seismica.v5i1.1809

Seismic Array Measurements in the Italian Candidate Site for the Einstein Telescope, the Third-Generation Gravitational Wave Detector

Giovanni Diaferia [*1], **Marco Olivieri** [1], **Irene Molinari** [1], **Annalisa Allocca** [4,5], **Enrico Calloni** [4,5], **Giovanni Luca Cardello** [6,3,2], **Andrea Contu** [3], **Domenico D'Urso** [6,3,2], **Rosario De Rosa** [4,5], **Matteo Di Giovanni** [8,9], **Luciano Errico** [4,5], **Luca Naticchioni** [10,2], **Davide Rozza** [11,12], **Lucia Trozzo** [5], **Carlo Giunchi** [2]

[1]Istituto Nazionale di Geofisica e Vulcanologia, Sezione di Bologna, Italy, [2]Istituto Nazionale di Geofisica e Vulcanologia, Sezione di Pisa, Italy, [3]INFN, Sezione di Cagliari, Italy, [4]Università degli Studi di Napoli Federico II, Napoli, Italy, [5]INFN, Sezione di Napoli, Italy, [6]Università degli Studi di Sassari, Sassari, Italy, [7]INFN, Sezione di Cagliari, Italy, [8]Scuola Normale Superiore, Pisa, Italy, [9]INFN, Sezione di Pisa, Italy, [10]INFN, Sezione di Roma, Italy, [11]INFN, Sezione di Milano-Bicocca, Milano, Italy, [12]Università degli Studi di Milano-Bicocca, Milano, Italy

Author contributions: *Conceptualization*: G. Diaferia, C. Giunchi, M. Olivieri, D. D'Urso. *Methodology*: G. Diaferia. *Software*: G. Diaferia. *Validation*: G. Diaferia. *Formal Analysis*: G. Diaferia. *Investigation*: G. Diaferia. *Resources*: E. Calloni, A. Contu, D. D'Urso, L. Naticchioni, D. Rozza, L. Trozzo, L. Errico, M. di Giovanni, A. Allocca. *Writing - Original draft*: G. Diaferia. *Review & Editing*: G. Diaferia, G.L. Cardello, C. Giunchi, M. Olivieri, I. Molinari. *Visualization*: G. Diaferia. *Supervision*: C. Giunchi, M. Olivieri, I. Molinari. *Project administration*: C. Giunchi. *Funding acquisition*: C. Giunchi.

Abstract Geophysical investigations and studies on the local seismic noise are of paramount importance for evaluating the candidate locations for hosting *Einstein Telescope* (ET), the third-generation gravitational wave detector. In the Italian candidate site, several active and passive geophysical acquisitions have been carried out, mainly focusing on the imaging of the shallow subsurface, while a full characterization of the noise wavefield was lacking. In this work, we present the results from three temporary seismic arrays installed at the Italian candidate site, each with different geometrical layouts, recording durations, and total numbers of stations. Here, we provide an overview on the seismic noise characteristics and its azimuthal distribution, obtained through beamforming. Moreover, we leverage the noise recordings to extract (i) Rayleigh wave dispersion curves using fk analysis, which are then inverted to obtain a one-dimensional, shear-wave velocity model of the subsurface and (ii) HVSR spectra across all arrays' stations. The recordings confirm the exceptionally low level of seismic noise approaching Peterson's New Low Noise Model for frequencies > 1 Hz. The arrays allowed to reliably reconstruct the seismic wavefield in the 10–20 Hz range, showing an almost azimuthally homogeneous noise source distribution, with slowness values between 0.4 and 0.5 s/km. The inversion of dispersion curves in the same frequency range highlighted a rather homogeneous, high-velocity terrain ($V_S = 2$–3 km/s) in the first 100 m. The flat HVSR spectra across all arrays excludes the presence of a resonant, low-velocity layer at shallow depth.

Production Editor: Yen Joe Tan
Handling Editor: György Hetényi
Copy & Layout Editor: Tara Nye

Received: September 29, 2025
Accepted: March 13, 2026
Published: April 22, 2026

1 Introduction

The area near the dismissed underground mine of Sos Enattos, located in the Sardinia island (Italy), has gained significant interest in the physics and geophysics community over the last decade. The low population density, the minimal seismic activity, and the absence of relevant anthropogenic activities provide an exceptionally low level of natural and man-made seismic noise. Such unique conditions are ideal for hosting scientific experiments which require high seismic quietness. In fact, the Sos Enattos underground mine hosted several scientific experiments so far. The SAR-GRAV laboratory was established, thanks to the partnership between Istituto Nazionale di Fisica Nucleare (INFN), Istituto Nazionale di Geofisica e Vulcanologia (INGV), Università degli Studi di Sassari, Università degli Studi di Cagliari, Regione Autonoma della Sardegna (RAS) and IGEA Spa (the company managing the mine activities).

Since 2022, a collaboration that currently involves more than 30 countries and approximately 1700 scientists have been working on the study, development, and design of the *Einstein Telescope* (ET), the third-generation gravitational wave detector (Punturo et al., 2010). With 10–15 km-long laser interferometers, most likely with an L-shaped configuration at 100–300 m depth for optimal noise suppression (Hutt et al., 2017), ET will reach a detectability threshold as low as a few Hz for the incoming gravitational waves, which are generated by cosmic events such as the coalescence of binary black holes and supernova explosions. In 2023, Italy formalized the candidacy to host ET in the Sos Enattos area (Fig. 1) due to the favorable, low noise conditions in the seismic, acoustic, and magnetic domains.

To support the candidacy of the Sardinia site, the *ET Italia* consortium (composed of a wide group of Italian research institutes and universities, including INGV, INFN, and the University of Sassari and Cagliari) conducted a variety of seismic surveys in the area. Saccorotti et al. (2023) employed a 13-node, $\sim$ 300 aper-

*Corresponding author: giovanni.diaferia@ingv.it

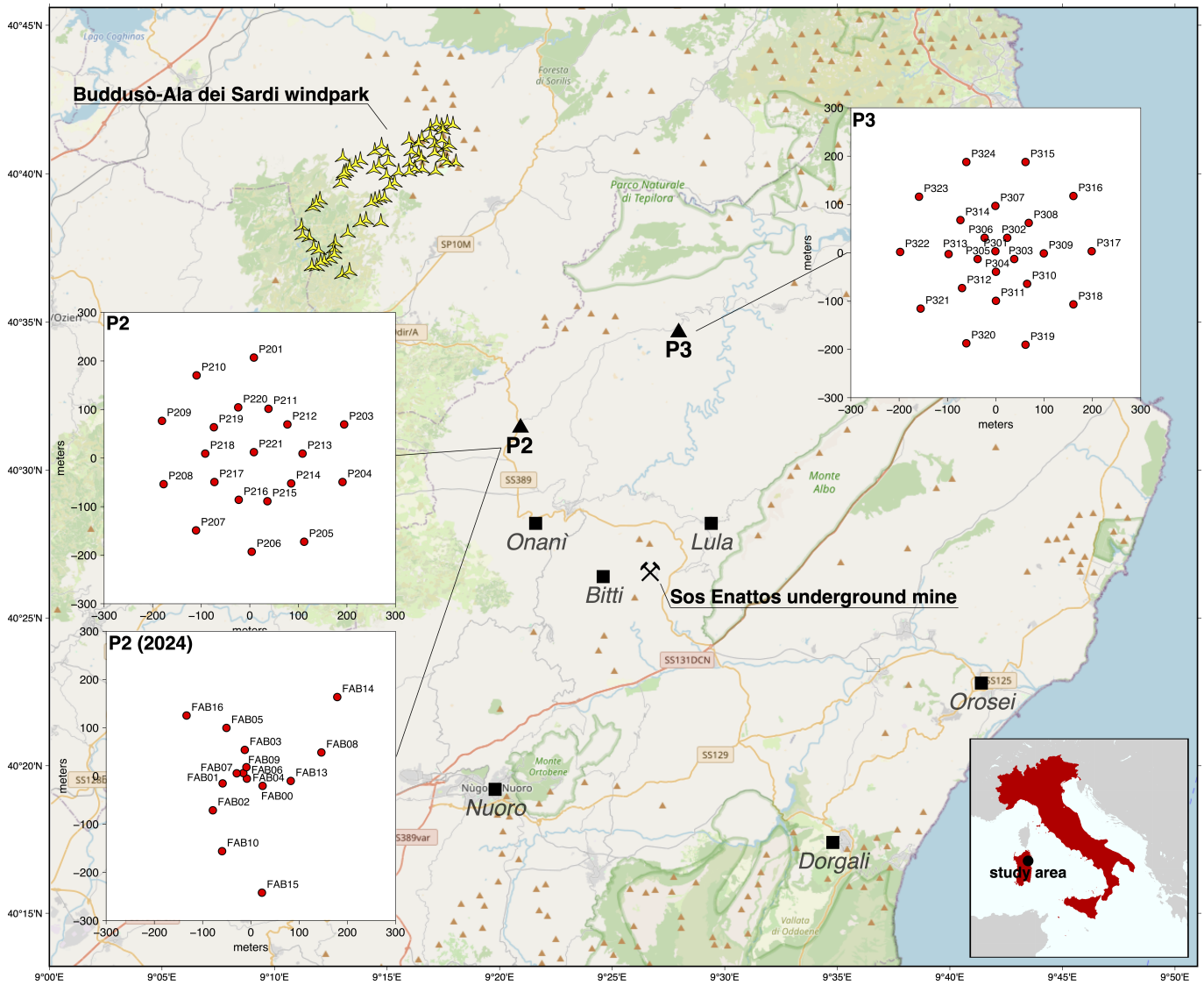

Figure 1 Map of the Italian candidate site for ET, in the vicinity of the dismissed underground mine of Sos Enattos (Sardinia, Italy). P2 and P3 are the locations of two permanent stations equipped with both surface and borehole sensors ($\sim$ 250 m depth). The insets show the configuration of the seismic arrays installed in 2021 at P2 and P3, and at P2 in 2024.

ture array in the close vicinity of the Sos Enattos underground mine, obtaining a shear wave velocity model of the shallow subsurface ($\sim$ 150 m depth) through the extraction of a Rayleigh wave dispersion curve. In Villani et al. (2025) a variety of refraction and reflection seismic, borehole logging, and ERT are described, which contributed to the understanding of the shallow subsurface in terms of seismic velocities and electrical resistivity. Diaferia et al. (2024) evaluated the contribution of a wind park to the overall seismic noise budget in the candidate site. However, an assessment of the spatial distribution of noise sources was lacking. For this reason, several array experiments have been conducted, which are presented and discussed in this study. In the following sections, we provide the details regarding the data acquisition, the methods employed, and the results. The noise spectral content is estimated using Probabilistic Power Spectral Densities (PPSD), while the spatial noise source distribution is evaluated through beamforming. Moreover, we use the Horizontal-to-Vertical Spectral Ratio (HVSR) and dispersion curves obtained by fk analysis to characterize the shallow subsurface at the site. Finally, we provide a discussion of the results, the lessons learned, and their impact on the characterization of the Italian candidate site for ET.

2 Geological and Geophysical setting

The study area (Fig. 1) lies within the Variscan crystalline basement of NE Sardinia which forms a plateau at approximately 900 m above sea level. The bedrock consists of meta-sedimentary units and orthogneisses (Carmignani et al., 2012). During the Carboniferous–Permian period, these rocks were intruded by granitoids (Casini et al., 2015) showing acidic and basic dikes. The regional succession comprises batholithic granitoids, gneisses, migmatites, micaschists, paragneisses with mylonitic fabrics, Lodè–Mamone orthogneisses, garnet-bearing schists, and metasandstones at Sos Enattos. Syntectonic metamorphic ages of 340–315 Ma (Di Vincenzo et al., 1994) constrain the

Array name	Array type	No. of stations	Recording length	Type of sensors
P2	concentric	20	10 days	Trillium Compact (TC) 120 s and TC 20 s
P3	concentric	24	10 days	TC 120 s, Trillium Post Hole 20 s and Lennartz MkIII
P2 (2024)	spiral	15	1 day	TC 120 s and TC 20 s

Table 1 Description of the arrays installed at Italian candidate site for ET. The map of the study area and the spatial layout of each array is shown in Fig. 1.

tectono-metamorphic evolution. Post-tectonic acidic dikes and intrusive bodies, such as the Sos Canales granitoid (310–290 Ma; Di Vincenzo et al., 1994), further increase the structural heterogeneity of the plateau. The crystalline basement exhibits widespread late- to post-Variscan brittle deformation, with joint, dyke, and fault sets. As recently supported by multidisciplinary studies (Villani et al., 2025), these structures have a strong influence on fluid circulation, weathering patterns, and mechanical properties. The transition from soil or weathered granite to unweathered bedrock occurs within a horizon that is 10–30 m thick. From a hydrogeological perspective, weathered granitoids and fractured zones act as small, localized aquifers. Geophysical surveys provide essential information about the subsurface architecture. Compressional seismic velocities exceed 5000 m/s in intact crystalline rocks and decrease in fractured domains, which is consistent with electrical resistivity patterns. In the ET candidate sites (see details in Section 3), high-resolution seismic refraction tomography and electrical resistivity tomography (Villani et al., 2025), calibrated by borehole logs, imaged the weathered layer and the crystalline basement down to a depth of 100–240 m. High V_P (5000–5500 m/s) and high resistivity ($> 1000\ \Omega$ m) at > 150 m depth indicate competent, weakly fractured rocks. In contrast, sub-vertical low-V_P (4250–4500 m/s) and low-resistivity ($< 500\ \Omega$ m) anomalies, 15–35 m wide, correspond to fracture zones with shallow groundwater. This is consistent with faults that have been mapped on the surface. From a seismological perspective, Sardinia is one of the least active regions of Italy, with only sparse low-magnitude events and a maximum offshore magnitude of $M_W \sim 5.1$ recorded in 1948 (Meletti et al., 2020); all the most significant seismic clusters identified historically and instrumentally occur offshore or along the coasts, at distances exceeding 100 km from the study area.

3 Array description and data acquisition

The area of interest comprises two of the potential vertices (labeled P2 and P3, Fig. 1) of the ET interferometer. Here, INFN has installed permanent pairs of surface and borehole sensors at 264 (P2) and 252 m (P3) depth since September 2021. The first campaigns consisted in the installation of temporary seismic arrays at the P2 site (18–28/09/2021), for a total recording length of 10 days. A second campaign was carried out at P3 (2–13/10/2021), for a total recording length of 11 days. In both cases, a concentric configuration was chosen (see Fig. 1), with 20 stations at P2 and 24 stations at P3, with a similar aperture of ~ 400 m for the two arrays. At P2, half of the stations were equipped with sensors Trillium Compact (TC) 120 s, while the other half with TC 20 s. At the P3 site, a combination of TC 120 s, Trillium Post Hole 20 s, and Lennartz LE-3Dlite MkIII were used. In both cases, seismic data were recorded with a 100 Hz sampling rate.

All the employed sensors have flat response in the entire frequency range investigated in this study (1–40 Hz). For the TC 120 s and 20 s (https://nanometrics.ca/hubfs/Downloads/Data%20Sheets/trillium_compact.png, last access January 2026) self-noise is near or below the Peterson's New Low Noise Model (NLMN, (Peterson, 1993)), while the LE-3Dlite MkIII (https://manuals.reftek.com/assets/pdfs/Lennartz_Sensors/Lennartz_Sensors.png, last access January 2026) represents an exception, with a self noise that is 25 dB higher than the Peterson's NLNM between 1 and 10 Hz.

A third, 24-hours long campaign was carried out at P2 (20–21/11/2024), opting for a 15-elements, three-arm, expanding spiral configuration with similar aperture ($\sim$ 430 m) as the previous ones. Such configuration was chosen as it is suggested to provide an adequate spatial sampling of the seismic wavefield, even with a limited the number of stations (Kennett et al., 2015; Tkalčić, 2015). The majority of the stations were equipped with TC 120 s, while three consisted in TC 20 s. To ensure the seismometers' thermal stability and minimize wind disturbance, the sensors were installed underneath 20–40 cm of soil. Also, in this case, the sampling rate was 100 Hz. For all three acquisition campaigns, the choices regarding the array aperture and layout are a compromise between the need to properly study the seismic noise characteristics (that were largely unknown at the time) and the limited accessibility to the sites. In Table 1 we summarize the configuration details for all the arrays. The theoretical capabilities and limitations of each array type can be quantitatively inferred on the basis of their aperture D and minimum station distance dx (Rost and Thomas, 2009; Schweitzer et al., 2012). In Tables 2, 3, and 4, we provide the ratio between the array aperture (D) and dominant wavelength (λ), maximum resolvable frequency (f_{max}), and the min–max resolvable wavenumbers (k_{min} and k_{max}). The tables refer to the case of different frequencies, being 3, 10 and 20 Hz, with propagation velocities of 3500, 2500 and 2000 m/s, respectively. At 3 Hz, the dominant wavelength is almost three times the aperture of each of the arrays, implying that none of these is able to correctly sample the propagating wavefield (i.e. each array reduces to a single station with respect to such large wavelength). On the contrary, for frequencies of 10 and 20 Hz, the aperture of each of the arrays are about half and a third of

array	geometry	wavelength/aperture ratio	max. non-aliased freq. [Hz]	min. wavenumber [m^{-1}]	max. wavenumber [m^{-1}]
		λ/D	$f_{max} = v/(2\,dx)$	$k_{\min} \sim 2\pi/D$	$k_{\max} \sim 2\pi/dx$
P2	aperture (D): 400 m min. dist (dx): 50 m	2.92	35	0.0157	0.1256
P3	aperture (D): 400 m min. dist (dx): 34 m	2.92	51	0.0157	0.1847
P2 (2024)	aperture (D): 430 m min. dist (dx): 9 m	2.71	194	0.0146	0.6978

Table 2 Array resolution parameters assuming a plane wave traveling at $v = 3500$ m/s with a frequency of 3 Hz.

array	geometry	wavelength/aperture ratio	max. non-aliased freq. [Hz]	min. wavenumber [m^{-1}]	max. wavenumber [m^{-1}]
		λ/D	$f_{max} = v/(2\,dx)$	$k_{\min} \sim 2\pi/D$	$k_{\max} \sim 2\pi/dx$
P2	aperture (D): 400 m min. dist (dx): 50 m	0.63	25	0.0157	0.1256
P3	aperture (D): 400 m min. dist (dx): 34 m	0.63	37	0.0157	0.1847
P2 (2024)	aperture (D): 430 m min. dist (dx): 9 m	0.58	139	0.0146	0.6978

Table 3 Array resolution parameters assuming a plane wave traveling at $v = 2500$ m/s with a frequency of 10 Hz.

array	geometry	wavelength/aperture ratio	max. non-aliased freq. [Hz]	min. wavenumber [m^{-1}]	max. wavenumber [m^{-1}]
		λ/D	$f_{max} = v/(2\,dx)$	$k_{\min} \sim 2\pi/D$	$k_{\max} \sim 2\pi/dx$
P2	aperture (D): 400 m min. dist (dx): 50 m	0.25	20	0.0157	0.1256
P3	aperture (D): 400 m min. dist (dx): 34 m	0.25	29	0.0157	0.1847
P2 (2024)	aperture (D): 430 m min. dist (dx): 9 m	0.23	111	0.0146	0.6978

Table 4 Array resolution parameters assuming a plane wave traveling at $v = 2000$ m/s with a frequency of 20 Hz.

the wavelength, providing a sufficient sampling of the wavefield. According to the Nyquist theorem, each array can correctly sample the wavefield only up to a certain frequency, above which aliasing starts to occur. Such limit is a function of the propagation velocity and the minimum station distance, and for P2 and P3, is suggested to be around $\sim$ 20–35 Hz. On the contrary, the spiral array at P2 (2024), having a minimum inter-station distance as low as $\sim$ 9 m, allows (in theory) to push the limit of non-aliased frequencies above 100 Hz (however, temporal aliasing occurs above 50 Hz due to the 100 Hz sampling frequency of the acquired seismic data). Another advantage of the spiral array is the very wide range of resolvable wavenumbers, as a consequence of the large range of inter-station distances that characterize such configuration. Based on these (theoretical) considerations, the three arrays are expected to be inadequate for frequencies below 10 Hz and higher than 20 Hz, except for the spiral array that could be able to correctly sample higher frequencies.

However, to correctly evaluate the actual capabilities of the arrays in terms of slowness and backazimuth resolution, thus accounting for the true array layout and number of stations, we calculate the Array Transfer Function (ATF), shown in Fig. 2, for the three reference frequencies as above (3, 10, and 20 Hz), spanning slowness differences of ± 2 s/km. Given the relatively small aperture, all arrays show the highest slowness resolution in the high-frequency range (10–20 Hz). Conversely, at lower frequency (3 Hz) the slowness retrieval is, as expected, characterized by larger uncertainties, approaching 1 s/km. Due to its higher number of stations, the array at P3 shows the higher azimuthal resolution and no or very weak side lobes appear at the three considered frequencies. The array at P2 shows slightly lower performance due to the fewer stations, while the spiral array at P2 (2024), having the lowest number of stations (15), shows the strongest side lobes and relatively poorer azimuthal resolution among the three arrays. It is worth mentioning that the ATF reflects the array performance under ideal conditions and, in reality, poor installation conditions and/or station malfunctioning can degrade the overall capability of a given array in the reconstruction of the incoming seismic wavefield. On the basis of the analysis above, the three arrays are expected to provide an adequate reconstruction of the seismic wavefield strictly in the 10–20 Hz range, with high uncertainties in the slowness retrieval (i.e. wide beam in the ATF) and strong aliasing below and above this range, respectively. Given the similar performance of the three arrays, the study allows to evaluate the possible contribution of the noise condition, site characteristics, recording length, and array layout in the retrieval of i) noise source distribution and amplitude, ii) propagation velocities, iii) geophysical model of the subsurface. Ultimately, such comparison can contribute to the evaluation of the best acquisition strategy depending on the intended purpose.

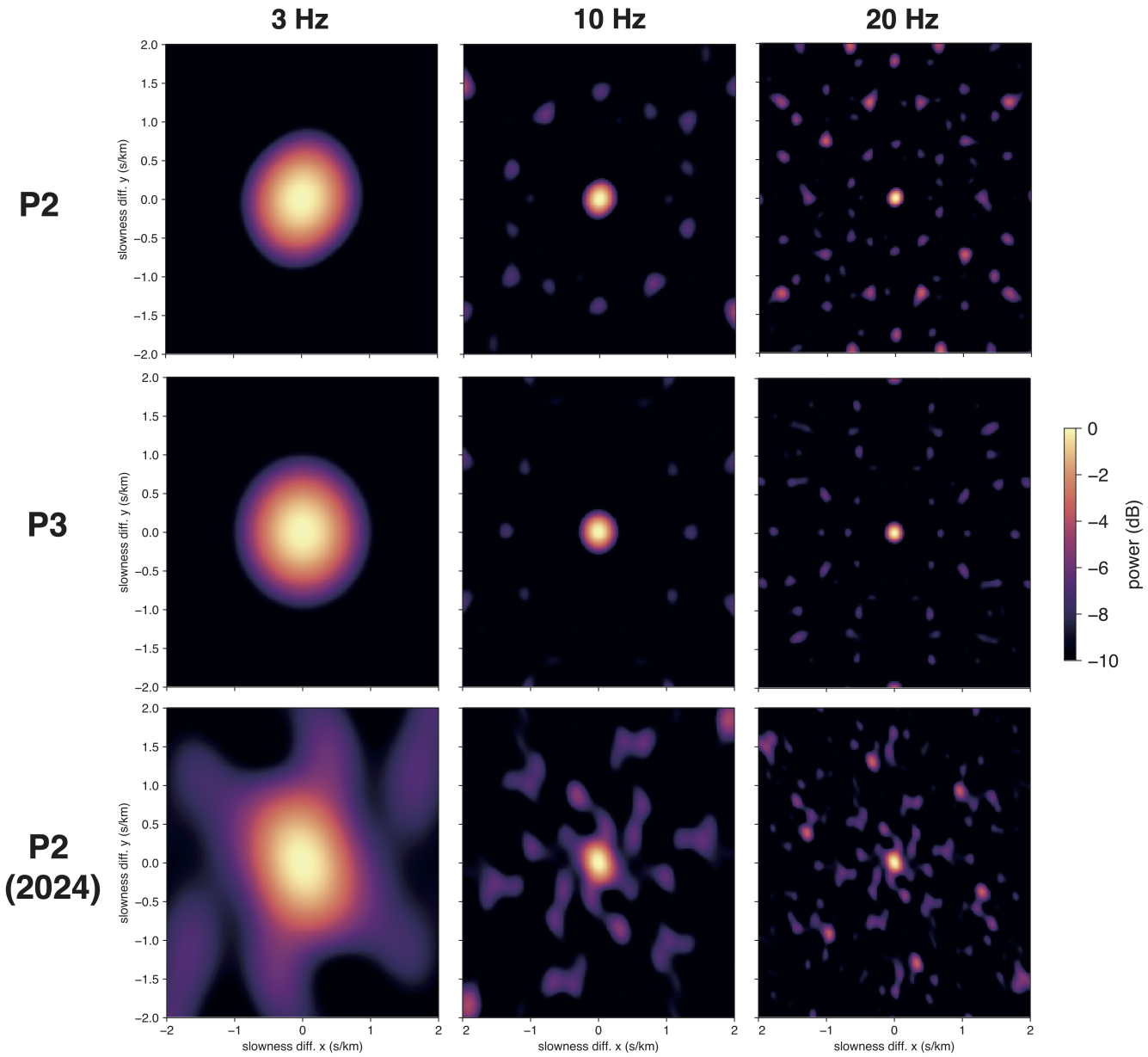

Figure 2 Array Transfer Function (ATF) for the P2, P3 and P2 (2024) arrays, calculated for frequencies centered at 3, 10, and 20 Hz. Details about the spatial array configurations are found in Table 1 and Fig. 1.

4 Methods and Results

4.1 Spectral analysis

For a first evaluation of data quality and spectral content, we use the entire recording length of the three arrays to produce Probabilist Power Spectral Density (PPSD) plots. In Fig. 3, these are given for three randomly selected stations in each array. For P2, a total of three sensors showed recording issues (i.e. faulty sensor). It can be observed that most of the recorded signal is in the 0.2–3 Hz range (Fig. 3a). Frequencies in the 3–10 Hz range are less represented and approach the Peterson's NLNM (Peterson, 1993). This testifies the seismic quietness of the area and the lack of any major natural and/or anthropogenic seismic noise sources above 1 Hz. A very low noise level is evident also at the P3 array (Fig. 3b). The array placed at P2 in 2024 (Fig. 3c), shows again that most of the noise is confined below 1 Hz, with an amplitude level which is about 10 dB higher than that previously recorded in the same location. Also at higher frequencies, stronger noise is recorded compared to P2 and P3. We explain such higher noise level in both the high- and low-frequency range with the stormy weather offshore Sardinia (wave height approaching 4 m, source *CMDS*) and strong wind bursts affecting the P2 site during the seismic campaign in 2024. In Fig. 4, we show the median spectra of all stations composing each array. Except for the three faulty sensors at P2, all stations across the three arrays show overlapping spectra in the entire low-frequency range (< 3 Hz). Spectra slightly diverge at higher-frequencies up to 40 Hz, especially at P2 (2024), likely reflecting the variability in wind exposure and in the installation conditions. At P3, the only station with a higher noise level starting from 3 Hz is the one with equipped with the Lennartz LE-3Dlite MkIII sensor, characterized by a significantly higher self-noise

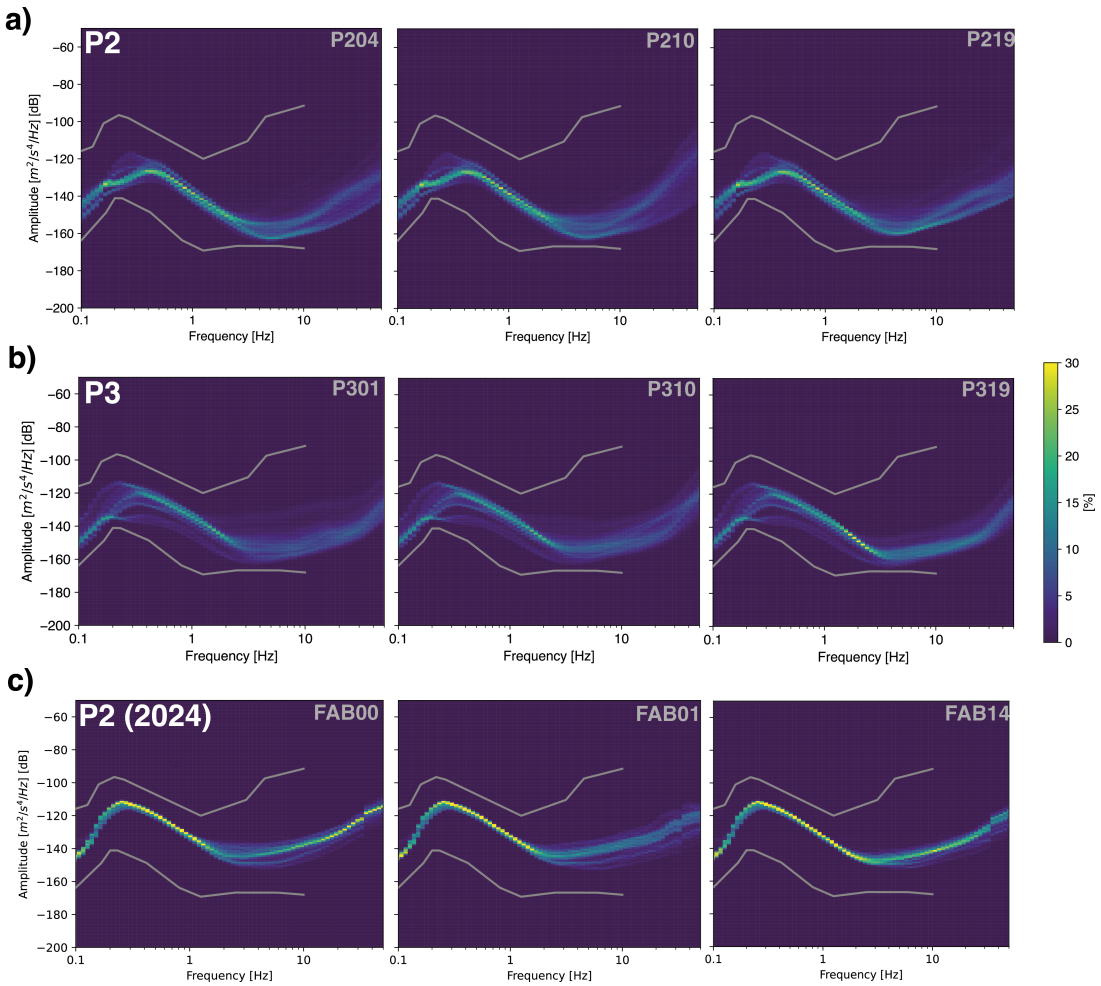

Figure 3 Probabilistic Power Spectral Density (PPSD) for three randomly selected stations of the arrays (a) P2, (b) P3, and (c) P2 (2024). Grey curves indicate the Peterson's New Noise Model (Peterson, 1993).

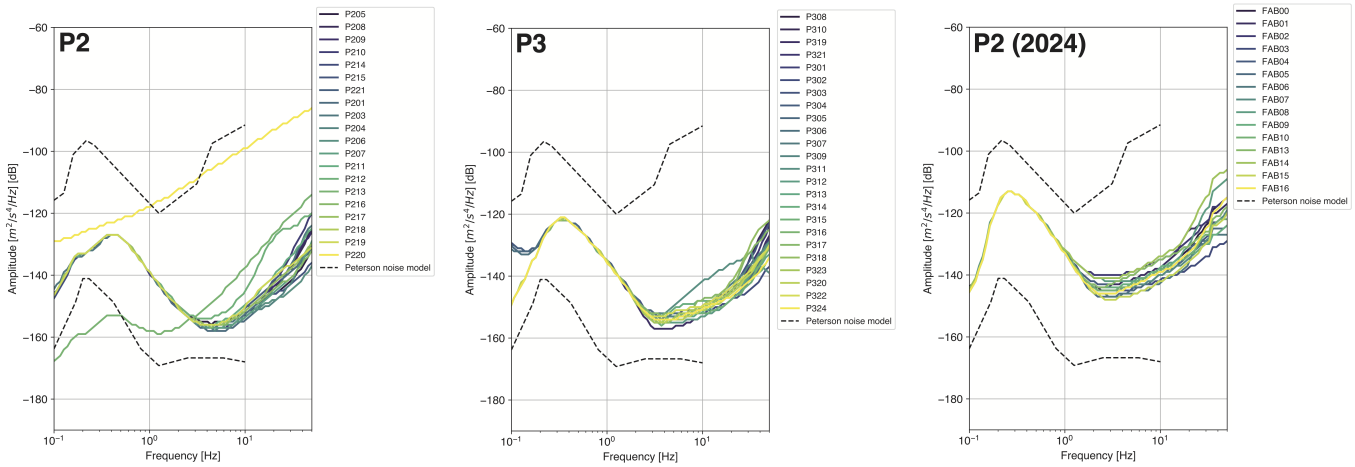

Figure 4 Median of the PPSD for all stations composing the arrays P2, P3 and P2 (2024). Dashed curves indicate the Peterson's New Noise Model (Peterson, 1993).

with respect to the other sensor employed in this study (see Section 3).

4.2 Beamforming

To estimate the direction of the incoming seismic noise, we apply a semblance-based beamforming procedure. Assuming a far-field, plane wave propagation, we employ an fk analysis approach (Kvaerna and Ringdahl, 1986) using a moving window on narrow band-passed filtered data X_j (with $j = 1, 2, ..., N$, N being the number of stations) around a central frequency ω_i (with $i = 1, 2, ...M$ for a total of M frequencies). Following Neidell and Taner (1971) and Douze and Laster (1979), for each frequency-wave number pair, the signal coherence is estimated by:

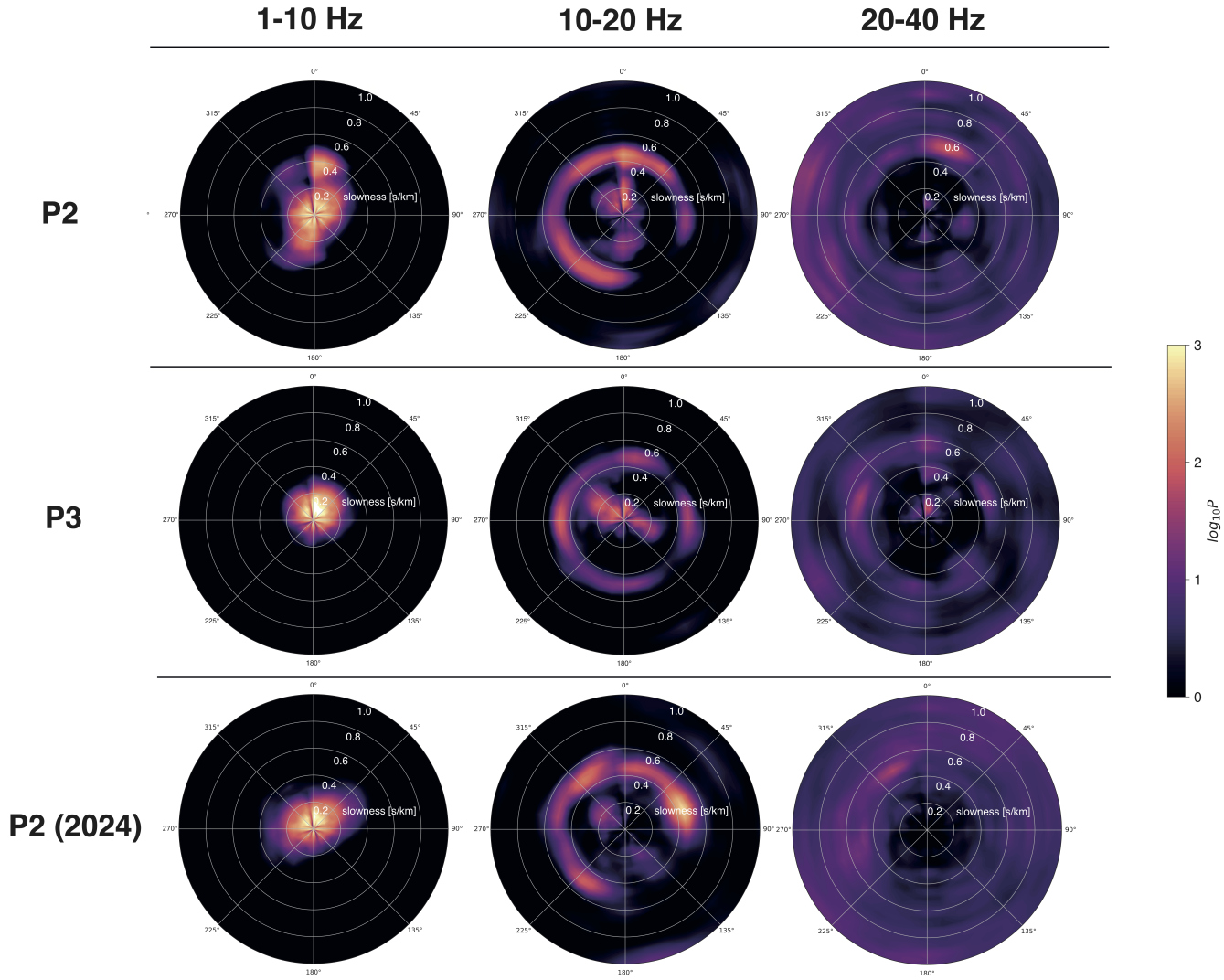

Figure 5 Results of the beamforming analysis for the arrays P2, P3 and P2 (2024) across thee different frequency bands (1–10, 10–20 and 20–40 Hz).

$$C(\omega,\vec{k}) = \frac{\sum_{i=1}^{M}\left|\sum_{j=1}^{N} X_j(\omega_i)e^{i\omega_i\vec{k}\cdot\vec{r}_j}\right|^2}{\sum_{i=1}^{M}\sum_{j=1}^{N}\left|X_j(\omega_i)e^{i\omega_i\vec{k}\cdot\vec{r}_j}\right|^2} \quad (1)$$

A grid-search approach is used to span the range of possible slowness (s) and backazimuth (θ) values, both related by:

$$\theta = \arctan\left(\frac{k_y}{k_x}\right) \quad \text{and} \quad s = \frac{|\vec{k}|}{\omega} \quad (2)$$

with k_x and k_y being horizontal components of the wavenumber. We run the beamforming analysis for a total of one day, randomly selected from the entire recording period at P2 and P3. For P2 (2024), we analyze the entire 24 hours of continuous recording available at this array.

In Fig. 5, we show the results of the beamforming analysis for the vertical component in three different frequency ranges, being 1–10, 10–20, and 20–40 Hz (see figures SM1–SM3 in the supplemental material for the beamforming results in 1 Hz narrow band). In the 1–10 Hz range, the three arrays show very similar results, with most of the beampower (expressed in logarithmic scale) that is confined in the northern sector and within 0.2 s/km. Only P2 shows some signal emerging with slowness $\sim$ 0.4 s/km, from the NNE and SSW direction. The low frequency and low-to-very low slowness suggest that this frequency range is mostly dominated by upward-propagating body waves, impinging the array with large apparent velocities (as high 0.1 km/s). In the 10–20 Hz range, according to the theoretical capabilities of the arrays and their ATF (see Fig. 2), the three arrays are expected to provide optimal results in terms of slowness and azimuthal resolution. At P2, the incoming noise is almost uniformly distributed across the entire azimuth range, except for the SE sector ($90-180°$), where no incoming signal is recorded. The slowness of the recovered signal is uniform with azimuth and mostly between 0.4–0.5 s/km, corresponding to 2–2.5 km/s. Based on this evidence, we conclude that this signal is mainly ambient noise propagating in the form of high-frequency Rayleigh waves. We explain the lack of noise source incoming from SE as a combination of two elements. Three roads border the P2 site (as close as $\sim$ 220 m) and cover the entire 0–45° (N to NE) and

180–360° (S to N) azimuth ranges, which are also those where most of the noise is recorded. Moreover, these areas show a dense tree coverage (*Quercus suber*, cork oak). By contrast, in the SE sector, roads are absent and tree coverage becomes sparser. Interestingly, the array P2 (2024) confirms the same slowness and directions of the incoming noise, including the absence of noise sources in the SE sector. The recovery of such consistent results using arrays that differ significantly in geometrical layout, number of stations, and time of deployment confirms i) the spatial invariance of the noise source distribution with time and ii) the effectiveness of the spiral array in recovering the same slowness and azimuthal properties of the wavefield as a concentric array with more stations. However, the P2 (2024) array shows only a major discrepancy with the earlier P2 deployment: a stronger signal incoming from ENE that corresponds to a heavily wooded area adjacent to the array. We deduce that such tree coverage, combined with the strong wind condition during the recording period (see the relatively higher noise level in the PPSD, Fig. 3c), might be regarded as the source of the strong signal emerging from ENE. This interpretation is supported by the lack of anthropic activities that could otherwise act as noise source and by the necessity for such source to be be fairly close to the array in order to produce a detectable signal, given the high damping of the seismic wavefield for frequencies above 10 Hz (Diaferia et al., 2024). Regarding the P3 array, we observe an almost homogeneous noise distribution with azimuth and having slowness between 0.4–0.5 s/km, similar to range estimated with the two arrays at P2, suggesting similar propagation velocities at the two sites. Interestingly, higher signal amplitudes emerge from the NW sector and with lower slowness, probably associated with higher-mode surface waves. Lastly, moving to the 20–40 Hz range, we do not observe a sufficiently coherent reconstruction of any slowness/backazimuth pairs for all three arrays. For P2 and P3, this can be caused by the inadequacy of the array design (i.e. relatively large inter-station distance) as spatial aliasing would occur for frequencies above 20–30 Hz (see Table 4). However, the array P2 (2024), despite the short inter-station distance (as low as 9 m as compared to 50 and 34 m of the previous arrays) that largely push the limit of the maximum resolvable frequency, shows the same beamforming results as at P2 and P3, indicating that these are due to the stochastic and/or incoherent nature of the seismic wavefield rather than caused by an inadequate spatial sampling.

4.3 Horizontal-to-Vertical spectral ratios

The Horizontal-to-Vertical Spectral Ratios (HVSR) is a fast and cost-effective method to estimate the resonance frequency of a certain site. According to Lachetl and Bard (1994) and Lermo and Chávez-García (1993), in an idealized model of a layer over a half-space, a strong impedance contrast in the subsurface generates high amplitudes in the horizontal components with respect to the vertical one, at a frequency (f_0) that closely resembles the site's fundamental resonance frequency (Nogoshi, 1971; Nakamura, 1989). The depth of the impedance contrast is related to f_0 by $f_0 = V_S/4h$, where V_S is the shear velocity above the interface and h is the thickness of the uppermost resonant layer. We followed the best practices for the extraction of HVSR (Havenith et al., 2004), consisting in the recording of seismic noise for a few minutes to hours, subdivision of the recorded data in time windows (commonly at least 30 seconds long), calculation of the spectral ratio in the frequency domain and averaging the spectra estimated in each time window. We employ the code `hvsrpy` (Vantassel, 2024), a Python implementation of the HVSR method based on Cheng et al. (2020, 2021); Cox et al. (2020), using six hours long recording at all stations composing the three arrays. Data are subdivided in 100 s-long time windows, and the spectra of the horizontal components are combined through geometric mean. Finally, the HVSR spectra are calculated in the $1-20$ Hz interval and averaged across all time windows. In Fig. 6 we show the HVSR spectra retrieved at each station composing the P2, P3, and P2 (2024) arrays. In each panel, the mean spectra (dashed black curve) and its 1σ dispersion across the whole array are reported. Starting with P2, the spectral ratios near the unity indicate no amplification at all stations. At P2, also the data recorded in 2024 confirms a substantially flat amplification spectra. Interestingly, a minor departure from unity (but approaching values that remain well below 1.5) is observed between 2 and 3 Hz. In addition, more dispersion around the mean spectra is present, especially for frequencies below 10 Hz. A possible explanation for such (even if small) discrepancies between the two arrays at the same site can be found in the different noise conditions during the two recording periods, both in terms of i) amplitude (see Fig. 3) and ii) wind gust disturbance at P2 (2024) that might affect the HVSR spectra (Mucciarelli, 1998; Mucciarelli and Gallipoli, 2001; Havenith et al., 2004). It is worth noting that a meteorological station was installed before the seismic acquisition at the P2 (2024) array and the recorded wind speed never exceeded 5 m s^{-1}, thus assuring the compliance with the best practice for the retrieval of HVSR (Havenith et al., 2004). Another reason for the possible discrepancies in the HVSR spectra among the three arrays can be found in possible and complex energy partitioning between Rayleigh, Love, and body waves (Bonnefoy-Claudet et al., 2008). Regarding the P3 array, all stations here show strongly overlapping and flat HVSR spectra, with an average close to unity and with very limited dispersion across the stations composing the array. Only two stations (P308 and P317) show a substantial departure for a flat site response, with a HVSR amplitude as high as 7 and 5 at 5 and 6 Hz, respectively. Given the strong discrepancy of these spectra with respect to the rest of the array, we suspect that these two stations suffered from unfavorable installation conditions. Overall, the flat HVSR spectra observed across all three arrays indicate a rather homogeneous shallow subsurface, with no major velocity contrasts and resonance effects, as suggested by the complementary geological and geophysical evidences presented in Section 2.

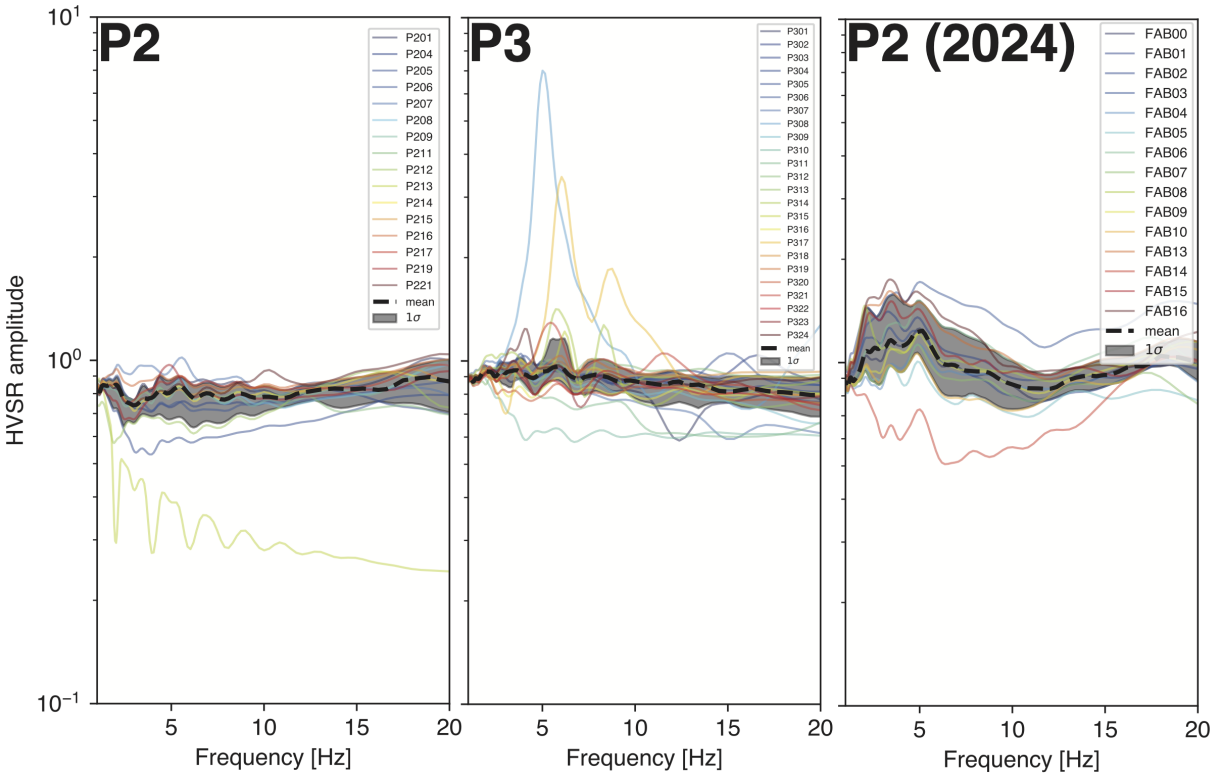

Figure 6 HVSR amplitude spectra extracted from a 6 hours-long recording at all stations composing the arrays P2, P3 and P2 (2024). The black dashed curve indicates the mean HVSR spectra at each array, together with the 1σ dispersion (shaded area).

4.4 fk-analysis and V_S model retrieval

The coherency measure introduced in Eq. 1 using the formulation of Neidell and Taner (1971) and Douze and Laster (1979) can be leveraged for constructing frequency(f)–wavenumber(k) plots, which are then converted to frequency–phase velocity (c) using the relation $|\vec{k}| = 2\pi f/c$. We perform the fk analysis using the Geopsy package (Wathelet et al., 2020), with 6 hours of continuous recording in the 6:00-12:00 time interval. We span the entire 1–30 Hz range, with a step of 0.1 Hz and 0.01 rad/m in the frequency and wavenumber domains, respectively. Results are shown in Fig. 7a, where we also show the picked dispersion curve in the frequency–phase velocity plane. All three arrays allow the retrieval of the Rayleigh wave fundamental mode mostly between 10 and 20 Hz, which is the same interval where all arrays have optimal resolution according to their aperture, inter-station distance, and ATF (Fig. 2). The picked phase-velocities in the 2-3 km/s range are also coherent with the slowness range estimated through beamforming (Fig. 5), comprised between 0.4 and 0.5 s/km in all three arrays. Interestingly, the array at P2 allows the picking of shear-wave velocities for frequencies as low as 3 Hz, though with higher uncertainties due to the limitations imposed by the array configuration. In contrast, the array P2 (2024) does not allow the recovery of phase velocities below 8 Hz due to the high ambiguity associated with the picks, likely caused by the suboptimal array configuration of the spiral array for such frequencies (i.e. shorter inter station distances). Even worse is the case for array P3, which does not allow any recovery of phase-velocities in the low-frequency range. Here, despite the good resolving power testified by the transfer function and their lack of any appreciable side lobes (see the ATF at 3 and 10 Hz in Fig. 2), the phase velocity–frequency plot suffers from very low beampower and smearing effects, likely due to the very low level of correlated background noise (see the PPSD in Fig. 3), that strongly hampers the retrieval of phase velocity dispersion curves through fk analysis. This is substantiated by a steep drop of the signal coherence (Welch, 1967) at P3 and P2 (2024) as a function of frequency (0.1 at 5 Hz and 3 Hz for P3 and P2 (2024), respectively; see supplemental figure SM4), indicating the prevalence of random, uncorrelated noise that dominates the recording of the closely-spaced sensors at these arrays. Particularly for the P3 array, the low coherence in combination with the extremely low level of the seismic background noise at all frequencies can explain the difficulty in the retrieval of the phase velocity dispersion curves through fk analysis. Interestingly, the P2 array show a less severe loss of coherence with frequency (0.1 at 12 Hz), and, as a consequence, it allows an easier extraction of the phase–velocity dispersion curve through fk analysis. We invert the picked dispersion curves with a trans-dimensional, Monte Carlo Markov Chain algorithm (Magrini et al., 2025). No *a priori* model parametrization (e.g. number of layers) is required, as it is inferred from the posterior sampling (Agostinetti and Malinverno, 2010; Bodin et al., 2012). In our case, the inversion of dispersion curves is expected to image the first 100–150 m, according to the sensitivity analysis

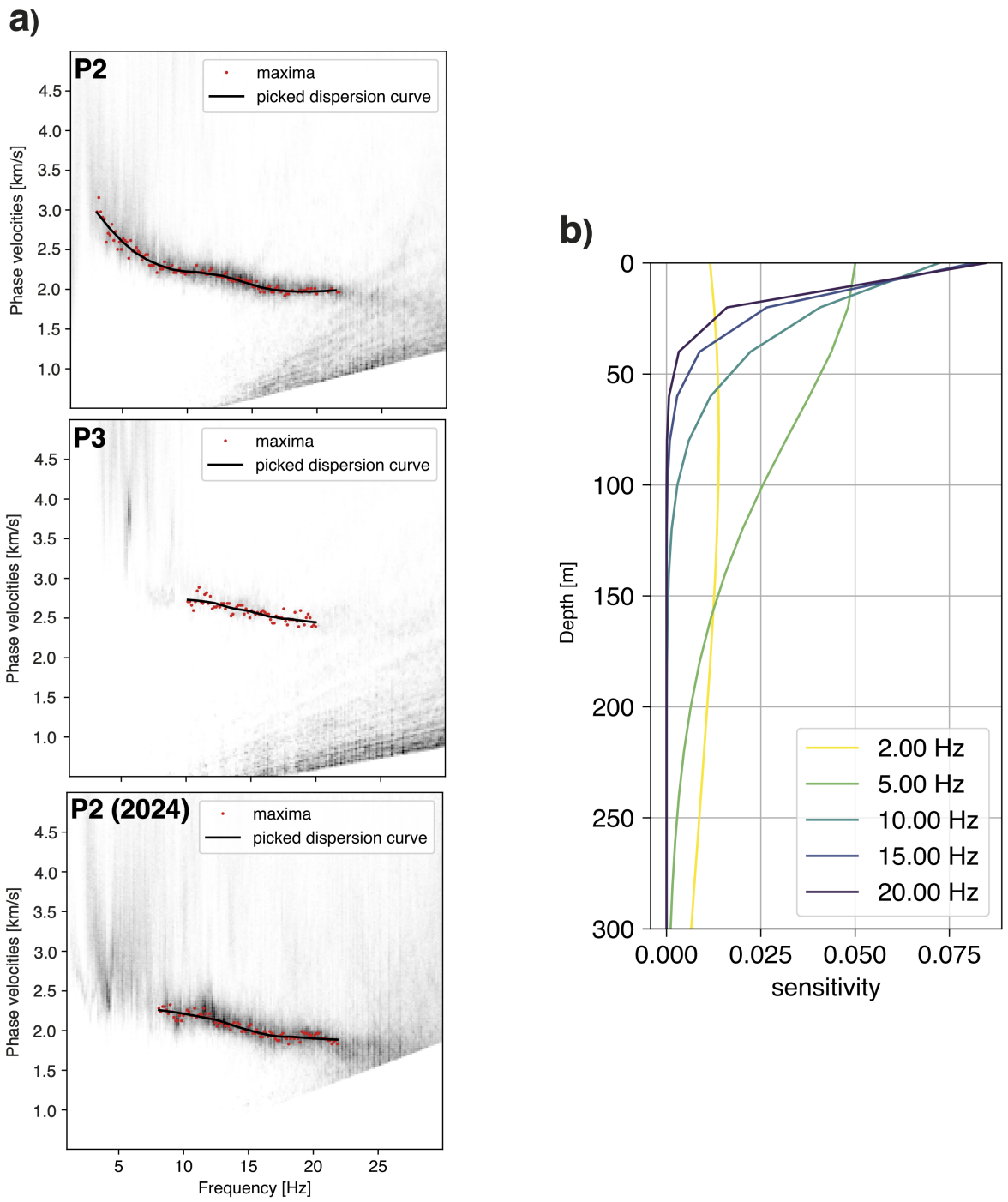

Figure 7 (a) Phase-velocities/frequency plot retrieved from fk analysis at the P2, P3 and P2 (2024) arrays. Dispersion curves are picked from power maxima, which are then fitted and resampled. (b) Sensitivity kernels for Rayleigh wave at different frequencies, on the assumption of a 400 m thick, layered medium with linearly increasing V_S from 2 to 4 km/s.

shown in Fig. 7b, where we provide the sensitivity kernels at 2, 5, 10, 15, and 20 Hz, assuming a 400 m thick layered medium with linearly increasing shear-wave velocities between 2 and 4 km/s. Since the picked dispersion curves mostly span the 10–20 Hz interval, we expect the data inversion to be informative for the first 50–100 m or less. Each dispersion curve is inverted using a uniform Gaussian prior of a three-layer model over a half-space. The total Markov Chain length is $250,000$ iterations, using 24 parallel chains. For each chain, models are retained every 100 steps to construct the ensemble of the posterior distribution, after a burn-in phase of $150,000$ iterations. In Fig. 8a–c, we show the ensemble solutions (and their mean and median) for the three arrays, together with the data fit and the posterior probability in terms of number of layers at each depth bin. The models from P2 and P2 (2024) show a high degree of similarity, with a 60–70 m thick layer of V_S in the 2–2.5 km/s range. Higher velocities up to 3 km/s are found at greater depth. At P3, as suggested already by the higher phase-velocities in the dispersion curves, the layer at 2 km/s is relatively thinner (30 m) than in P2, and shear-wave velocities rapidly increase to 3 km/s. The inverted models suggest a roughly homogeneous subsurface, as

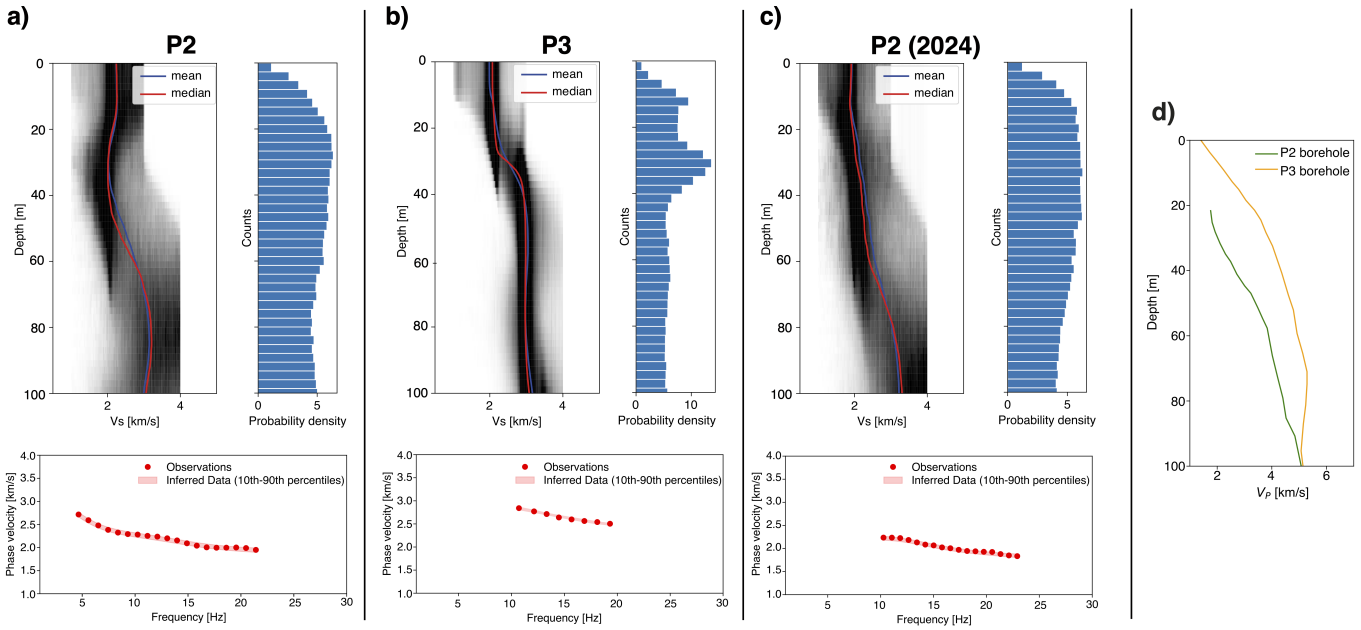

Figure 8 One dimensional V_S models in terms of posterior probability density function, obtained from MCMC inversion of the Rayleigh wave dispersion curves for the array at (a) P2, (b) P3, and (c) P2 (2024). In each panel, i) the histograms indicate the probability of having an interface at each depth and ii) the bottom plot provides the dispersion curves at each array and the fit in terms of 10–90th percentile. d) P-wave velocities extracted along the boreholes at the P2 and P3 sites, modified from Villani et al. (2025).

also indicated by the almost flat probability of having a velocity transition at each depth bin, with velocities that moderately increase with depth and are mostly confined in the 2–3 km/s range. The relatively high velocity recorded at shallow depth is coherent with the absence of any low-velocity resonant layer, as already pointed out by the HVSR analysis in Section 4.3. As a comparison, we show in Fig. 8d the 1-D, high-resolution V_P profiles from borehole data at P2 (green line) and P3 (orange line), modified from Villani et al. (2025). Considering the depth above the resolved region (dashed lines) as indicated by Villani et al. (2025), we observe that P-wave velocities rapidly reach high values ($\sim$ 5 km/s) within the first tens of meters. Though with its inherently lower resolution, the models from fk analysis confirm the same high velocity trend in the shallow subsurface, confirming the relatively higher velocities encountered at P3 compared to P2.

5 Discussion

The Italian candidate site for ET has been investigated using three seismic arrays, in order to estimate the characteristics of the local seismic noise and characterize the shallow subsurface of the area. The first two arrays were installed in 2021, recording for a total of 10 days at two different locations (P2 and P3, see Fig. 1), using 20 and 24 stations, respectively, in a concentric configuration, with an aperture of $\sim$ 400 m. In 2024, a new array acquisition was carried out at P2, recording for only one day, using fewer stations (15) in a spiral layout and an aperture which is comparable to that of the previous arrays. The PPSD plots testify that P2 and P3 have very similar seismic noise characteristics, as it is mostly confined in the 0.2–3 Hz range. In the higher frequency range, the noise levels approach the NLNM, thus confirming the seismic quietness of the area in the anthropogenic range, implying lack of any major noise source. Noisier spectra ($>$ 10 dB) are observed at P2 (2024), both in the low-frequency and high-frequency ranges, due to a combination of stormy weather offshore and persistent wind at the site. This contrasting observation at the P2 site confirms the importance of long-lasting recording (several weeks or months) for a correct evaluation of the noise spectral characteristics at a site, accounting for the temporal amplitude variation of the noise source.

We used beamforming to leverage the multi-station configuration of the arrays and reconstruct the direction of arrival of the seismic noise at the sites. The analysis of the ATF suggests that the geometrical layouts of the three arrays (Fig. 2) are optimal for reconstructing the seismic wavefield only in the range 10–20 Hz. In this frequency interval, the incoming seismic wavefield is confined in the 0.4–0.5 s/km slowness range, uniformly distributed in azimuth, except for the SE sector, from which no incoming noise is recorded. Interestingly, despite the reduced number of sensors employed at P2 (2024), this array provided highly similar results to P2 (20 stations, 30% more), indicating that the spiral array configuration is highly efficient, providing adequate resolution at the cost of a reduced number of sensors. Considering the similarity of the beamforming results between P2 and P2 (2024) in the 10–20 Hz range, despite the different conditions of the overall noise level, we suggest that noise source distribution is here mostly time-invariant. It follows that short recording lengths (e.g. one day) would suffice for the sole reconstruction of the velocity and azimuthal distribution

of seismic noise. In the 20–40 Hz range, the seismic noise appears largely incoherent, almost uniformly distributed in slowness and azimuth. The suboptimal resolving power of the arrays in this frequency range, as indicated by the ATF 2, does not allow a further assessment of the noise characteristics, which would require a proper smaller aperture array.

Lastly, for the 1–10 frequency range, the beamforming shows that high-velocity seismic noise mostly comes from the northern sector, strongly dominated by upward propagating body waves. This observation is utterly important for a correct estimation of the total seismic budget for ET, in particular regarding the so-called Newtonian noise, i.e. the seismic disturbance related to tiny density anomalies that are generated by seismic waves propagating through heterogeneous media Beker et al. (2010); Harms (2019); Badaracco and Harms (2019). However, for an improved reconstruction of the seismic wavefield, specifically in the 1–10 Hz range, which is the operational range for ET, a larger aperture array is advised with longer recording periods (e.g. months), to capture possible seasonal variation (e.g. offshore sea-wave, storms) affecting the noise distribution. By fk analysis, we retrieved the Rayleigh wave dispersion curves that, according to the aperture characteristics of the three arrays, mostly cover the 10–20 Hz range, showing phase-velocities that overlap with the slowness values obtained through beamforming. The array at P2 showed slightly higher capabilities with respect to P2 (2024) in retrieving phase velocities toward the lower frequency range, mainly due to the higher slowness resolution shown in the ATF (see Fig. 2). Particularly instructive is the case of the P3 array that, despite the optimal slowness and azimuthal resolution testified by its ATF, made retrieving the Rayleigh wave dispersion curve particularly difficult. We believe that the reason for such poor performance is to be found in the extremely low level of seismic noise rather than in the configuration of the array, which is optimal for the reconstruction of the seismic wavefield in this frequency range (see ATF in Fig. 2). The inversion of the picked dispersion curves range has allowed us to image only the shallow subsurface within 100 m depth. Relatively high and homogeneous shear-wave velocities (2–3 km/s) are retrieved, in accordance with the known *a priori* knowledge of the local terrain, which consists of unfractured orthogneiss and granitoid rocks (Carmignani et al., 2012). A confirmation of the rather uncomplicated geological setting at the array sites emerges from the HVSR spectra. The flat HVSR curves obtained across the entire extent of the arrays indicate an areally homogeneous (at least at the scale of the array aperture), non-amplifying geological terrain, with no low-velocity resonant layer at shallow depth.

5.1 Suggestions and lesson learned

This study allowed a comparison of three arrays with different spatial layouts, number of stations, and recording lengths at two sites with very low levels of natural and man-made noise, providing not only valuable insights into the seismic noise characteristics (i.e. amplitude and spatial distribution), but also concerning the performance of different acquisition strategies. This is particularly valuable for better planning the perspective, large-scale geophysical characterization of the ET candidate site. Given the very low noise level in the area, the extraction of valuable information from passive recordings can be challenging, as shown by our attempt to derive phase-velocities dispersion curves from fk analysis at P3, despite the optimal array configuration. Given the homogeneity of the shallow subsurface, as suggested by the HVSR spectra and the inversion of phase-velocity dispersion curves, active methods (e.g. reflection and refraction seismic) are expected to be poorly informative, due to the lack of major lithological/structural discontinuity at depth. If a full, three-dimensional, high-resolution velocity model is sought, long-term passive recording with a dense array might represent a viable solution. A sufficient number of cross-correlation stacks between each station, ensured by a sufficiently long recording (several months), would likely compensate for the very low noise level of the area. However, for the sole characterization of the seismic noise and its source distribution, seismic arrays are an adequate choice, once the stations' layout and recording length are tailored to the frequency of interest. In our case, the 400 m aperture has been proven to be optimal in the 10–20 Hz and enabled a full, high-resolution reconstruction of the noise slowness and source distribution through beamforming. For targeting lower frequencies (i.e. 1–10 Hz), the array should have an aperture which is three-four times larger than that employed in this study. A spiral array configuration was shown to be particularly efficient and cost-effective, providing comparable results to those obtained with a concentric layout and a higher number of stations. We observed that for the sake of solely characterizing the noise source distribution, a one-day-long recording might suffice. On the contrary, the construction of reliable and representative noise spectra requires longer recordings, to account for possible diurnal variation and change in weather conditions.

6 Conclusion

In this study, we presented and analyzed the datasets from three temporary seismic arrays acquired at the Italian candidate site for ET, the third-generation gravitational wave detector. We used spectral analysis, beamforming, fk analysis, and HVSR to evaluate and characterize both natural and man-made seismic noise as well as the local subsurface. Moreover, we assessed the suitability of three different array configurations for future data acquisition campaigns in the area, in light of the target frequency ranges for ET. It follows a list of the main findings:

1. All three array acquisitions confirm the exceptionally low level of seismic noise (close to the Petersons' NLNM) for frequencies above 1 Hz. P2 (2024), which is the array that recorded for 24 hours, was affected by a relatively higher level of noise due to the unfavorable weather condition (strong

wind), thus highlighting the importance of long-term recording that allows to account for temporal variation in noise level.

2. The $\sim$ 400 m aperture of the arrays was proven to be optimal only for the 10–20 Hz range, where we successfully reconstructed the azimuthal noise source distributions and slowness through beamforming. We found an almost homogeneous source distribution in azimuthal. The 1–10 Hz range is characterized by very high apparent velocities, suggesting the prevalence of body waves. However, for an adequate beamforming analysis below 10 Hz a larger aperture array is advised.

3. HVSR and inversion of Rayleigh wave dispersion curve suggest a fairly homogeneous shallow subsurface, characterized by high shear-wave velocities ($2000 - 3000$ m/s) and no resonant layer.

Acknowledgements

This study was conducted within the framework agreement between Istituto Nazionale di Fisica Nucleare (INFN) and Istituto Nazionale di Geofisica e Vulcanologia (INGV). The study was financed by INFN in the frame of the collaboration agreement with INGV Accordo di Programma per la Conduzione di Studi e Ricerche Finalizzati alla Caratterizzazione Geofisica e Sismica del Sito di Sos Enattos (NU), thanks to the Protocollo di Intesa tra Ministero dell'Università e della Ricerca, Regione Autonoma della Sardegna, the Istituto Nazionale di Fisica Nucleare and the University of Studi di Sassari; by the Università degli Studi di Sassari thanks to the Accordo di Programma tra la Regione Autonoma della Sardegna, Università degli Studi di Sassari, l'Istituto Nazionale di Fisica Nucleare, l'Istituto Nazionale di Geofisica e Vulcanologia, l'Università degli Studi di Cagliari e l'IGEA S.P.A. (project SAR-GRAV, funds FSC 2014–2020, Patto per lo sviluppo della Regione Sardegna), to the Fondo di Ateneo per la ricerca 2019 and 2020, and to Fondazione di Sardegna, project 2022–2023: CUP-J83C21000060007. G. Diaferia acknowledges the NRRP-MEET (Monitoring Earth's Evolution and Tectonic, CUP D53C22001400005) project funded by NextGenerationEU.

Data and code availability

ObsPy (Beyreuther et al., 2010) was used for the processing of seismic data. Figures were made with PyGMT (Tian et al., 2026) and the Python library `matplotlib`. Seismic recordings of the P2 and P3 arrays are available on the EIDA repository (Danecek et al., 2021) under the network code 7P_2021 (link: https://eida.ingv.it/it/network/7P_2021). Seismic recordings for the P2 (2024) array are also available on EIDA, under the network code 3M_2024 (link: https://eida.ingv.it/it/network/3M_2024). The code `BayesBay` (Magrini et al., 2025) was used for the inversion of Rayleigh wave dispersion curves. Data from CMDS are available at https://data.marine.copernicus.eu/.

Competing interests

The author declare no competing interests.

References

Agostinetti, N. P. and Malinverno, A. Receiver function inversion by trans-dimensional Monte Carlo sampling. *Geophysical Journal International*, 2010. doi: 10.1111/j.1365-246x.2010.04530.x.

Badaracco, F. and Harms, J. Optimization of seismometer arrays for the cancellation of Newtonian noise from seismic body waves. *Classical and Quantum Gravity*, 36(14), 2019. doi: 10.1088/1361-6382/ab28c1.

Beker, M. G., Cella, G., DeSalvo, R., Doets, M., Grote, H., Harms, J., Hennes, E., Mandic, V., Rabeling, D. S., van den Brand, J. F. J., and van Leeuwen, C. M. Improving the sensitivity of future GW observatories in the 1–10 Hz band: Newtonian and seismic noise. *General Relativity and Gravitation*, 43(2):623–656, 2010. doi: 10.1007/s10714-010-1011-7.

Beyreuther, M., Barsch, R., Krischer, L., Megies, T., Behr, Y., and Wassermann, J. ObsPy: A Python toolbox for seismology. *Seismological Research Letters*, 81(3):530–533, 2010. doi: 10.1785/gssrl.81.3.530.

Bodin, T., Sambridge, M., Tkalčić, H., Arroucau, P., Gallagher, K., and Rawlinson, N. Transdimensional inversion of receiver functions and surface wave dispersion. *Journal of Geophysical Research: Solid Earth*, 117(B2), 2012. doi: 10.1029/2011jb008560.

Bonnefoy-Claudet, S., Kohler, A., Cornou, C., Wathelet, M., and Bard, P.-Y. Effects of Love Waves on Microtremor H/V Ratio. *Bulletin of the Seismological Society of America*, 98(1):288–300, 2008. doi: 10.1785/0120070063.

Carmignani, L., Conti, P., FUNEDDA, A. L., Oggiano, G., Pasci, S., et al. La geologia della Sardegna. *Geological field trips*, 4(2.2): 1–104, 2012.

Casini, L., Cuccuru, S., Puccini, A., Oggiano, G., and Rossi, P. Evolution of the Corsica–Sardinia Batholith and late-orogenic shearing of the Variscides. *Tectonophysics*, 646:65–78, 2015. doi: 10.1016/j.tecto.2015.01.017.

Cheng, T., Cox, B. R., Vantassel, J. P., and Manuel, L. A statistical approach to account for azimuthal variability in single-station HVSR measurements. *Geophysical Journal International*, 223(2), 2020. doi: 10.1093/gji/ggaa342.

Cheng, T., Hallal, M. M., Vantassel, J. P., and Cox, B. R. Estimating Unbiased Statistics for Fundamental Site Frequency Using Spatially Distributed HVSR Measurements and Voronoi Tessellation. *Journal of Geotechnical and Geoenvironmental Engineering*, 147 (8), 2021. doi: 10.1061/(asce)gt.1943-5606.0002551.

Cox, B. R., Cheng, T., Vantassel, J. P., and Manuel, L. A statistical representation and frequency-domain window-rejection algorithm for single-station HVSR measurements. *Geophysical Journal International*, 221(3):2170–2183, 2020. doi: 10.1093/gji/ggaa119.

Danecek, P., Pintore, S., Mazza, S., Mandiello, A., Fares, M., Carluccio, I., Della Bina, E., Franceschi, D., Moretti, M., Lauciani, V., Quintiliani, M., and Michelini, A. The Italian Node of the European Integrated Data Archive. *Seismological Research Letters*, 92(3):1726–1737, 2021. doi: 10.1785/0220200409.

Di Vincenzo, G., Ghezzo, C., and Tonarini, S. Geochemistry and Rb-Sr geochronology of the Hercynian peraluminous Sos Canales pluton (central Sardinia, Italy). *Comptes rendus de l'Académie des sciences. Série 2. Sciences de la terre et des planètes*, 319(7): 783–790, 1994.

Diaferia, G., Giunchi, C., Olivieri, M., Molinari, I., Di Felice, F., Contu,

A., D'Urso, D., Naticchioni, L., Rozza, D., Harms, J., Cardini, A., De Rosa, R., Di Giovanni, M., Mangano, V., Ricci, F., Trozzo, L., and Murineddu, C. Seismic noise characterisation for the Budusò – Ala dei Sardi wind park (Sardinia, Italy) and its impact on the Einstein Telescope candidate site. *EGUsphere*, 2024. doi: 10.5194/egusphere-2024-3600.

Douze, E. J. and Laster, S. J. Statistics of semblance. *Geophysics*, 44(12):1999–2003, 1979. doi: 10.1190/1.1440953.

Harms, J. Terrestrial gravity fluctuations. *Living Reviews in Relativity*, 22(1), 2019. doi: 10.1007/s41114-019-0022-2.

Havenith, H.-B. et al. Guidelines for the implementation of the H-V spectral ratio technique on ambient vibrations: measurements, processing and interpretation. Technical report, European Commission, 2004.

Hutt, C. R., Ringler, A. T., and Gee, L. S. Broadband Seismic Noise Attenuation versus Depth at the Albuquerque Seismological Laboratory. *Bulletin of the Seismological Society of America*, 107(3): 1402–1412, 2017. doi: 10.1785/0120160187.

Kennett, B. L. N., Stipčević, J., and Gorbatov, A. Spiral-arm seismic arrays. *Bulletin of the Seismological Society of America*, 105(4), 2015. doi: 10.1785/0120140354.

Kvaerna, T. and Ringdahl, F. Stability of various f-k estimation techniques. *Semiannual Technical Summary*, 1-86/87:29–40, 1986.

Lachetl, C. and Bard, P.-Y. Numerical and theoretical investigations on the possibilities and limitations of Nakamura's technique. *Journal of Physics of the Earth*, 42(5):377–397, 1994. doi: 10.4294/jpe1952.42.377.

Lermo, J. and Chávez-García, F. J. Site effect evaluation using spectral ratios with only one station. *Bulletin of the Seismological Society of America*, 83(5):1574–1594, 1993. doi: 10.1785/bssa0830051574.

Magrini, F., He, J., and Sambridge, M. BayesBay: A Versatile Bayesian Inversion Framework Written in Python. *Seismological Research Letters*, 96(3):2052–2064, 2025. doi: 10.1785/0220240275.

Meletti, C., Camassi, R., and Castelli, V. A Reappraisal of the Seismicity of Sardinia, Italy. *Seismological Research Letters*, 92(2A): 1148–1158, 2020. doi: 10.1785/0220200255.

Mucciarelli, M. Reliability and applicability of Nakamura's technique using microtremors: an experimental approach. *Journal of Earthquake Engineering*, 2(4):625–638, 1998. doi: 10.1080/13632469809350337.

Mucciarelli, M. and Gallipoli, M. R. A critical review of 10 years of microtremor HVSR technique. *Bollettino di Geofisica Teorica ed Applicata*, 42(3-4):255–266, 2001.

Nakamura, Y. A method for dynamic characteristics estimation of subsurface using microtremor on the ground surface. *Railway Technical Research Institute, Quarterly Reports*, 30(1), 1989.

Neidell, N. S. and Taner, M. T. SEMBLANCE AND OTHER COHERENCY MEASURES FOR MULTICHANNEL DATA. *GEOPHYSICS*, 36(3), 1971. doi: 10.1190/1.1440186.

Nogoshi, M. On the amplitude characteristics of microtremor, Part II. *Journal of the seismological society of Japan*, 24:26–40, 1971.

Peterson, J. R. Observations and Modeling of Seismic Background Noise. Open-File Report 93-322, U.S. Geological Survey, 1993. doi: 10.3133/ofr93322.

Punturo, M., Abernathy, M., Acernese, F., Allen, B., Andersson, N., Arun, K., Barone, F., Barr, B., Barsuglia, M., Beker, M., et al. The Einstein Telescope: A third-generation gravitational wave observatory. *Classical and Quantum Gravity*, 27(19):194002, 2010. doi: 10.1088/0264-9381/27/19/194002.

Rost, S. and Thomas, C. *Improving Seismic Resolution Through Array Processing Techniques*, page 3–31. Springer Netherlands, 2009. doi: 10.1007/978-90-481-3680-3_2.

Saccorotti, G., Giunchi, C., D'Ambrosio, M., Gaviano, S., Naticchioni, L., D'Urso, D., Rozza, D., Cardini, A., Contu, A., Dordei, F., et al. Array analysis of seismic noise at the Sos Enattos mine, the Italian candidate site for the Einstein Telescope. *The European Physical Journal Plus*, 138(9):793, 2023. doi: 10.1140/epjp/s13360-023-04395-2.

Schweitzer, J., Fyen, J., Mykkeltveit, S., Gibbons, S. J., Pirli, M., Kühn, D., and Kværna, T. Seismic arrays. In *New manual of seismological observatory practice 2 (NMSOP-2)*, pages 1–80. Deutsches GeoForschungsZentrum GFZ, 2012.

Tian, D., Leong, W. J., Fröhlich, Y., Grund, M., Schlitzer, W., Jones, M., Toney, L., Yao, J., Tong, J.-H., Magen, Y., Materna, K., Belem, A., Newton, T., Anant, A., Ziebarth, M., Quinn, J., He, X., Uieda, L., and Wessel, P. PyGMT: A Python interface for the Generic Mapping Tools, 2026. doi: 10.5281/ZENODO.18080259.

Tkalčić, H. Complex inner core of the Earth: The last frontier of global seismology. *Reviews of Geophysics*, 53(1):59–94, 2015. doi: 10.1002/2014rg000469.

Vantassel, J. jpvantassel/hvsrpy: v2.0.0, 2024. doi: 10.5281/ZENODO.12735911.

Villani, F., Maraio, S., Improta, L., De Martini, P., Cavallaro, D., Firetto Carlino, M., Brunori, C., Longo, V., Casini, L., Caradonna, M., Zei, C., Rapisarda, S., Oggiano, G., Giunchi, C., Saccorotti, G., Coltelli, M., D'Urso, D., Naticchioni, L., Ricci, F., Schillaci, G., Cittadino, D., Marsella, M., Napoleoni, Q., Rossini, C., and Cardello, G. Subsurface characterization of crystalline rocks at the Einstein Telescope candidate site (Italy): Insights from seismic tomography, geoelectrical and morphostructural analyses. *Tectonophysics*, 911:230830, 2025. doi: 10.1016/j.tecto.2025.230830.

Wathelet, M., Chatelain, J.-L., Cornou, C., Giulio, G. D., Guillier, B., Ohrnberger, M., and Savvaidis, A. Geopsy: A User-Friendly Open-Source Tool Set for Ambient Vibration Processing. *Seismological Research Letters*, 91(3):1878–1889, 2020. doi: 10.1785/0220190360.

Welch, P. The use of fast Fourier transform for the estimation of power spectra: A method based on time averaging over short, modified periodograms. *IEEE Transactions on Audio and Electroacoustics*, 15(2), 1967. doi: 10.1109/tau.1967.1161901.